mater.scichina.com link.springer.com

Published online 4 January 2021 | https://doi.org/10.1007/s40843-020-1553-8
Sci China Mater 2021, 64(6): 1427–1436

Lead-free halide perovskite $Cs_3Bi_2Br_9$ single crystals for high-performance X-ray detection

Xiang Li[1†], Xinyuan Du[2†], Peng Zhang[1], Yunqiu Hua[1], Lin Liu[1], Guangda Niu[2*], Guodong Zhang[1*], Jiang Tang[2] and Xutang Tao[1*]

ABSTRACT **All-inorganic lead-free halide perovskites have attracted interest owing to their high ambient and thermal stabilities, excellent optoelectronic properties, and environmental friendliness. Herein, the bismuth-based halide perovskite $Cs_3Bi_2Br_9$ single crystals were successfully grown to a diameter of 12 mm and length of 40 mm using a modified Bridgman method for the first time. The resistivity and transmittance of transparent and crack-free $Cs_3Bi_2Br_9$ single crystal are ~6.8×10^{11} Ω cm and ~80%, respectively. The carrier mobility of the (−120) plane is 0.17 $cm^2 V^{-1} s^{-1}$ along the [010] orientation (*b* axis), and the trap density is 9.7×10^{10} cm^{-3}. Moreover, $Cs_3Bi_2Br_9$ single crystals exhibit excellent potential for X-ray detection, including a high absorption coefficient, a superior X-ray sensitivity of ~230.4 μC Gy_{air}^{-1} cm^{-2}, and an ultra-low and no-drift dark current density of ~17.8 pA mm^{-2}, which enables lower noise and is also beneficial to the ultra-low detection limit for X-ray detectors. Our study shows that $Cs_3Bi_2Br_9$ is a promising candidate for X-ray detection applications.**

Keywords: all-inorganic halide perovskite, $Cs_3Bi_2Br_9$, single crystal growth, X-ray detection

INTRODUCTION

Halide perovskites have demonstrated great potential for energy conversion [1], photodetection [2,3], and nuclear radiation detection [4] owing to their useful optoelectronic properties [5], including a tunable band gap [6], high mobility [7], simple processing technique [8], and simple integration with various semiconductor materials [9]. Despite the merits of the lead-halide perovskite family, lead is dangerously toxic to the human body and biological systems owing to its high solubility in water and volatility in air [10–13].

Recently, less toxic metals such as tin, antimony, and bismuth have been widely investigated to replace lead for environmentally friendly requirements [14–16]. Among these, low-dimensional bismuth-halide materials have emerged as potential optoelectronic materials for the following reasons: (1) Bi is considered a 'green' element, which exhibits potential for mass production as an environmentally friendly compound [17]; (2) Bi^{3+} possesses an identical $6s^26p^0$ electronic structure with Pb^{2+}, and this expected electronic configuration and band dispersion may yield excellent optoelectronic properties, owing to spin-orbit coupling [18]; (3) inorganic bismuth-halides typically exhibit a higher-temperature and moisture stability than their organic-inorganic hybrid counterparts [10]; (4) the ionic activation energies of low-dimensional perovskites are significantly higher than those of three-dimensional (3D) $CsPbBr_3$, $Cs_2AgBiBr_6$, and $MAPbBr_3$, and this efficiently restrains the ionic migration in 2D layered crystals. Moreover, bismuth-halides have potential applications in photodetection and X/γ ray detection owing to their superior semiconductor properties such as a large effective atomic number *Z*, high resistivity, and an extremely low concentration of charge traps [4].

Some progress has been made in the growth and X-ray detection applications of bismuth-halide perovskite single crystals (SCs). Zhuang *et al.* [4] grew a layered $(NH_4)_3Bi_2I_9$ SC from a solution and demonstrated its X-ray detection performance with a very high sensitivity (*S*) of 8000 μC Gy_{air}^{-1} cm^{-2}, based on parallel device architecture. Zheng *et al.* [19] reported a solution-grown 0D $MA_3Bi_2I_9$ SC with an X-ray detection *S* as high as 10,620 μC Gy_{air}^{-1} cm^{-2}. Furthermore, hybrid perovskite $(BA)_2CsAgBiBr_7$ SCs (2D) and $(H_2MDAP)BiI_5$ SCs (1D) have been successfully grown from a solution, and *S* of 4.2

[1] State Key Laboratory of Crystal Materials, Institute of Crystal Materials, Shandong University, Jinan 250100, China
[2] Wuhan National Laboratory for Optoelectronics (WNLO), Huazhong University of Science and Technology (HUST), Wuhan 430074, China
[†] These authors contributed equally to this work.
[*] Corresponding authors (emails: guangda_niu@mail.hust.edu.cn (Niu G); zgd@sdu.edu.cn (Zhang G); txt@sdu.edu.cn (Tao X))

and 1 μC Gy_{air}^{-1} cm^{-2} were obtained, respectively [20,21]. In addition, all-inorganic 0D bismuth-halide $Cs_3Bi_2I_9$ SCs were grown using the Bridgman method and nucleation-controlled solution method in Xu's group [22] and Liu's group [23], respectively. X-ray detection *S* of 119 and 1652.3 μC Gy_{air}^{-1} cm^{-2} were achieved based on the melt-grown and solution-grown crystals, respectively [22,23]. The all-inorganic 2D $Rb_3Bi_2I_9$ SC was obtained using a solution with an *S* of 159.7 μC Gy_{air}^{-1} cm^{-2}, and the dark current density was less than 38.2 pA mm^{-2} [24]. In addition to the high *S* for X-ray detection, bismuth-halide perovskites with low dimensional structures exhibit high resistivity and very low ionic migration. This results in extremely low dark currents at the pA level and no drift, which is beneficial for an extremely low detectable dose rate [20–23,25].

All-inorganic $Cs_3Bi_2Br_9$ (space group $P\bar{3}m1$, a = 0.796 nm, c = 0.984 nm) is crystallized with a 2D layer structure [10]. It contains high-*Z* elements Cs, Bi, and Br, and has a high density of 4.7 g cm^{-3}. The average atomic number of $Cs_3Bi_2Br_9$ (46.1) is larger than that of α-Se (34), $MAPbBr_3$ (41.2), and $Cs_2AgBiBr_6$ (45), and is only slightly smaller than that of $(NH_4)_3Bi_2I_9$ (48.3) and $Cs_3Bi_2I_9$ (57.7). In addition, $Cs_3Bi_2Br_9$ also exhibits large band gaps (2.61 eV), which suggests its potential to achieve high resistivity and low leakage current when utilized as radiation-detecting materials. Several studies have reported the properties of $Cs_3Bi_2Br_9$ perovskite. Leng *et al.* [10] reported the millimeter-scale $Cs_3Bi_2Br_9$ SC, manufactured using a low-temperature solution method, and Ji *et al.* [26] reported the photodetection performances of $Cs_3Bi_2Br_9$ films. Moreover, $Cs_3Bi_2Br_9$ quantum dot also exhibits potential for blue light emission and photoluminescence with high quantum yields [27–29]. However, to date, the photoelectric properties and detection performances of $Cs_3Bi_2Br_9$ SCs have not been reported.

Herein, we report the growth of $Cs_3Bi_2Br_9$ bulk crystals (ϕ 12 mm × 40 mm) using a modified vertical Bridgman method. The optoelectronic properties, photon detection performance, and X-ray detection performance of melt-grown $Cs_3Bi_2Br_9$ SCs were systematically studied for the first time.

EXPERIMENTAL SECTION

Synthesis and single crystal growth of $Cs_3Bi_2Br_9$

High-purity CsBr (99.999% purity) and $BiBr_3$ (99.999% purity) purchased from Aladdin Chemistry Co. Ltd. with a stoichiometric ratio of CsBr:$BiBr_3$ = 3:2 were loaded into a silica ampoule, which was then evacuated to 4 × 10^{-4} Pa and sealed with an oxyhydrogen flame. The sealed ampoule was subsequently transferred to a well furnace controlled by a temperature controller (FP23, Shimaden, Japan). The furnace was slowly heated to 700°C at a rate of 70°C h^{-1}. After being maintained at this temperature for 30 h, the furnace was slowly cooled to 30°C at 20°C h^{-1}.

The synthesized polycrystalline $Cs_3Bi_2Br_9$ was re-sealed in a quartz ampoule (inner diameter: 12 mm) under vacuum conditions of 10^{-4} Pa for SC growth. After sealing, the quartz ampoule with polycrystalline $Cs_3Bi_2Br_9$ was transferred into a three-zone modified vertical Bridgman furnace. The temperatures of the upper, middle, and lower zones were set to 700, 600 and 400°C, respectively. The temperature gradient near the solid-liquid interface was 10–20°C cm^{-1}. To completely melt the polycrystalline $Cs_3Bi_2Br_9$, the ampoule was held in the high-temperature zone for 24 h. Then, the ampoule moved down slowly, at a speed of 0.5–3 mm h^{-1}, to a low-temperature zone. After solidification, the furnace temperature was cooled to room temperature (30°C) within 7 days, and bulk $Cs_3Bi_2Br_9$ SCs were obtained.

Crystal processing technology

The as-grown $Cs_3Bi_2Br_9$ crystals were oriented using an X-ray Laue diffractometer (MWL 120, MULTIWIRE LABORATORIES, Ltd.) and cut into 2-mm-thick wafers using an STX-202A diamond wire cutting machine. The surfaces of the wafers were polished with 7000 mesh sandpaper and polishing powder. In the final step, the surfaces of the samples were washed with alcohol to remove any residues.

Material characterizations

Thermogravimetric analysis (TGA) and differential scanning calorimetry were performed under N_2 flow from 30 to 700°C. X-ray diffraction (XRD) patterns of powders and SC plates were measured using an AXS D8 ADVANCE X-ray diffractometer (Bruker, Massachusetts, USA) with Cu Kα irradiation (λ = 1.54056 Å) in the range of 10°–90° (2θ) with a step size of 0.02° and scanning speed of 0.04 s per step. Scanning electron microscopy (SEM) and energy-dispersive X-ray spectroscopy (EDS) measurements were performed using a field emission scanning electron microscope (S-4800, Hitachi, Japan) with energy dispersive X-ray spectrometry (EMAX Energy EX-350, Horiba, Japan). Ultraviolet-visible diffuse reflectance spectroscopy was conducted using a UV-2550 spectrophotometer (Shimadzu, Japan) in the range of 200–900 nm; $BaSO_4$ was used as the reference sample.

Photoluminescence (PL) and lifetime measurements were performed using an FLS-980 apparatus (Edinburgh Instruments, UK). The ultraviolet-visible transmittance spectrum of the $Cs_3Bi_2Br_9$ plate was measured using an ultraviolet-visible spectrometer (U-4100, Hitachi, Japan) over a spectral range of 0.3–2.5 μm. A Fourier-transform infrared spectrometer (Spectrum 100, Perkin Elmer, USA) was used to measure the spectrum in the middle infrared range (2.5–18 μm). X-ray photoelectron spectroscopy (XPS) analysis was conducted using a monochromatic Al Kα source (1486 eV) created by an ESCALAB 250 XPS system (Thermo Fisher Scientific, USA) to study the composition of the samples. Current-voltage (*I-V*) and current-time (*I-T*) were measured using a semiconductor parameter analyzer (4200, Keithley Instruments, USA). A laser diode (LD) (2.97–14.9 mW mm^{-2}) with a wavelength of 430 nm was employed as the illumination source to measure the photoresponses. A tungsten anode X-ray tube (L9421-02, Hamamatsu, Japan) was used as the source, and it had a maximum output of 8 W and an X-ray focal spot size of 5 μm. The X-ray source was operated with a constant 50 kV acceleration voltage. A 2-mm-thick Al foil was inserted between the source and $Cs_3Bi_2Br_9$ SC X-ray detectors to serve as the attenuator to percolate the low-energy X-rays. The dose rate was changed by adjusting the X-ray tube current, and the dose rate was calibrated using an ion chamber dosimeter (MagicMax IBM, GER). A source meter (2635, Keithley Instruments, USA) was used to apply the bias voltage and record the response current. All measurements were performed at room temperature (30°C) in air.

RESULTS AND DISCUSSION

The left graph in Fig. 1a illustrates a schematic diagram of the homemade semitransparent vertical Bridgman furnace, with which the crystal growth parameters could be recorded and adjusted in real time during the growth process. The optimized temperature field for $Cs_3Bi_2Br_9$ SC growth is shown in the right graph of Fig. 1a. $Cs_3Bi_2Br_9$ SCs with a diameter of 12 mm and length of ~40 mm, which is the largest recorded bulk $Cs_3Bi_2Br_9$ SC, were grown using the modified Bridgman method for the first time. In the crystal growth experiments (Table S1), a small temperature gradient, slow growth rate, and cooling rate are crucial in avoiding structural defects and crystal

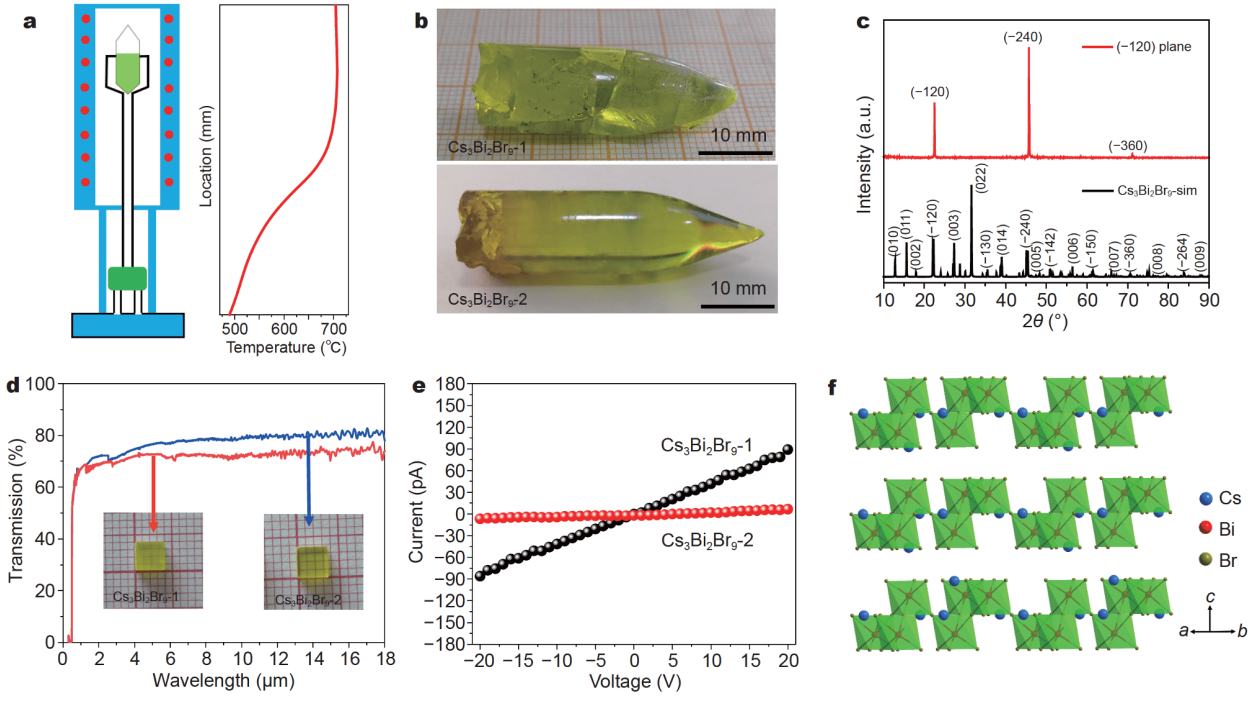

Figure 1 (a) Schematic diagram of vertical Bridgman furnace for $Cs_3Bi_2Br_9$ SC growth (left) and the optimized temperature field for $Cs_3Bi_2Br_9$ SC growth (right). (b) Photographs of the as-grown $Cs_3Bi_2Br_9$ SC-1 (upper) and $Cs_3Bi_2Br_9$ SC-2 (lower). (c) XRD patterns of (−120) plane. (d) Transmission spectra for (−120) planes of $Cs_3Bi_2Br_9$ SC-1 and $Cs_3Bi_2Br_9$ SC-2. Insets are the oriented (−120) planes of $Cs_3Bi_2Br_9$ SC-1 and $Cs_3Bi_2Br_9$ SC-2, respectively. (e) Resistivities for (−120) planes of $Cs_3Bi_2Br_9$ SC-1 and $Cs_3Bi_2Br_9$ SC-2. (f) Crystal structure of $Cs_3Bi_2Br_9$ (the red atoms are Bi, green atoms are Br, and blue atoms are Cs).

cracks and in favoring the growth of high-quality $Cs_3Bi_2Br_9$ SCs. Typically, a slower growth rate (0.5 mm h^{-1}) and cooling rate (4°C h^{-1}) were adopted for transparent and crack-free $Cs_3Bi_2Br_9$ SC-2 growth (bottom photograph in Fig. 1b), while a growth rate of 3 mm h^{-1} and cooling rate of 15°C h^{-1} were adopted for cracked $Cs_3Bi_2Br_9$ SC-1 (top photograph in Fig. 1b). The powder XRD pattern of the polycrystalline $Cs_3Bi_2Br_9$ was in good agreement with the pattern simulated from the SC data (Fig. S1a). After growth, the finely polished plates with a (−120) orientation (Fig. S1b) of $Cs_3Bi_2Br_9$ SCs were further confirmed by the XRD patterns (Fig. 1c).

Fig. 1d shows the optical transmittance spectra of the (−120) planes of $Cs_3Bi_2Br_9$ SC-1 and $Cs_3Bi_2Br_9$ SC-2 with a thickness of 2 mm. They exhibit a wide transparent range, from 0.3 to 18 μm, without obvious absorptions. The average transmittance of $Cs_3Bi_2Br_9$ SC-2, from 2 μm to more than 18 μm, is approximately 80%, which is greater than that of $Cs_3Bi_2Br_9$ SC-1 (~70%). In addition, the ultraviolet absorption edges of the as-grown $Cs_3Bi_2Br_9$ SC-1 and $Cs_3Bi_2Br_9$ SC-2, locate at 0.48 μm, corresponding to a bandgap of 2.57 eV (Fig. S2). Moreover, Fig. 1e shows a higher resistivity for the (−120) plane of $Cs_3Bi_2Br_9$ SC-2 (~6.8×10^{11} Ω cm) compared with that of $Cs_3Bi_2Br_9$ SC-1 (~5.1×10^{10} Ω cm). The high resistivity of $Cs_3Bi_2Br_9$ SC-2 decreases the dark current and noise current. TGA shows that $Cs_3Bi_2Br_9$ starts losing weight at ~500°C, and the weight decreases sharply after 598°C (Fig. S3), which is consistent with the boiling of $BiBr_3$ and sublimation of CsBr, respectively. Moreover, all inorganic perovskite $Cs_3Bi_2Br_9$ SCs are considerably more thermally stable than hybrid perovskites, such as $MA_3Bi_2I_9$ or $MA_3Bi_2Br_9$ SCs [10].

$Cs_3Bi_2Br_9$ crystallizes in the trigonal system ($P\bar{3}m1$ space group) at room temperature [10]; and its crystal structure is illustrated in Fig. 1f. Layered perovskite $Cs_3Bi_2Br_9$ can be viewed as a tripling of the traditional perovskite unit cell in which only two-thirds of the octahedral positions are fully occupied. Corrugated layers are composed of the rest of the octahedral sites, which remain vacant and segregated to realize $[BiBr_6]^-$ octahedral corner-sharing [30].

Owing to the 2D layered structure, a large thin $Cs_3Bi_2Br_9$ SC slice perpendicular to the [001] orientation can be easily split. The SEM image in Fig. 2a clearly shows the lamination structure of the thin $Cs_3Bi_2Br_9$ SC slice. According to the XPS results shown in Fig. 2b–d, the separated spin-orbital components (Δ) of Cs ($3d_{5/2}$, $3d_{3/2}$),

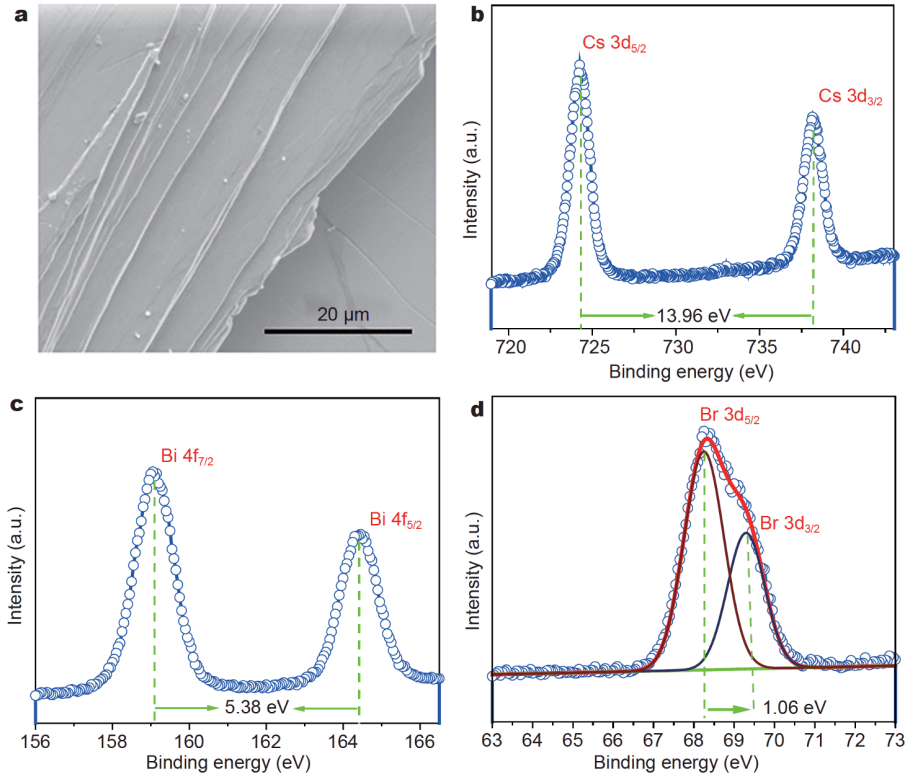

Figure 2 (a) SEM image of the layered structure for a $Cs_3Bi_2Br_9$ SC. (b–d) XPS spectra of a $Cs_3Bi_2Br_9$ SC: (b) Cs 3d, (c) Bi 4f, and (d) Br 3d.

Bi ($4f_{7/2}$, $4f_{5/2}$), and Br ($3d_{5/2}$, $3d_{3/2}$) were 13.96, 5.35, and 1.06 eV, corresponding to the valences of +1, +3, and −1, respectively [31]. Fig. S4 shows the XPS survey spectrum of $Cs_3Bi_2Br_9$ SC. In addition, the ratio of Cs, Bi, and Br was further confirmed by EDS, which revealed a ratio of Cs:Bi:Br = 2.6:2.0:9.3, which is consistent with the stoichiometric ratio of $Cs_3Bi_2Br_9$ (Fig. S5a). To study the elemental distribution, EDS mapping measurements were performed, and all elements of Cs, Bi, and Br were observed and distributed uniformly on the surface of the $Cs_3Bi_2Br_9$ SC (Fig. S5b–f).

Fig. 3a shows the ultraviolet-visible absorption spectrum and steady-state PL spectrum of the $Cs_3Bi_2Br_9$ powder. The inset is the Tauc plot curve converted by the Kubelka-Munk equation for the bandgap calculation [32]. The absorption spectrum of $Cs_3Bi_2Br_9$ exhibits a sharp absorption edge at 479 nm, indicating a direct bandgap feature. The corresponding bandgap of 2.61 eV is consistent with that reported by Leng *et al.* [10], which is slightly higher than the result calculated from the transmittance spectrum (2.57 eV). The PL spectrum of melt-grown $Cs_3Bi_2Br_9$ excited by 400 nm light reveals an emission peak at 479 nm, which is consistent with the absorption edge well. Moreover, our melt-grown $Cs_3Bi_2Br_9$ SC also exhibits a shoulder peak at ~496 nm, as mentioned for solution-grown $Cs_3Bi_2Br_9$ [10], which may be related with the defects introduced by grinding.

As shown in Fig. 3b, the time-resolved PL spectrum consists of three components. The short lifetime and intermediate components, which originate from the high trap density near the crystal surface yield τ_1 = 0.627 ns with 1.80% and τ_2 = 2.933 ns with 4.94%, respectively. However, the long-lived component, which correlates with the carrier recombination in defect-free bulk crystal, yields τ_3 = 94.31 ns with 93.26%. The calculated average lifetime is 88.1 ns, which is significantly larger than that of solution-grown $Cs_3Bi_2Br_9$ SC (15.9 ns), $Cs_3Bi_2Br_9$ quantum dots (14.1 ns), and melt-grown $CsPbBr_3$ SC (10.9 ns) [7,10]. This indicates that fewer defects exist in the melt-grown crystals [33].

The carrier-transport property of the $Cs_3Bi_2Br_9$ SC was determined for the first time using a space-charge limited current (SCLC) measurement with a simple sandwich structure of Au/$Cs_3Bi_2Br_9$ SC/Au. The current-voltage (I–V^n) curve of the $Cs_3Bi_2Br_9$ SC device, as shown in the inset of Fig. 4a, is divided into the Ohmic region (n = 1) between 0 and 44 V, trap-filling (TFL, n >3) between 44 and 68 V, and the Child region (n = 2) between 68 and 100 V. The current from the SCLC region is primarily moved by the injected charge carriers from the Au electrode. Therefore, the current depends only on the carrier mobility, which was calculated using the Mott-Gurney theory as follows [34]:

$$\mu = \frac{8J}{9\varepsilon_0\varepsilon}\left(\frac{L^3}{V^2}\right), \quad (1)$$

where μ is the carrier mobility and L is the length of the conductive device channel, J and V are the dark current density and applied voltage, respectively, and ε_r (average value of 11.75 in Table S2) and ε_0 are the relative dielectric constant and vacuum permittivity, respectively.

The trap-state density (n_{trap}) can be extracted according to the following equation:

$$n_{trap} = \frac{2\varepsilon_0\varepsilon_r V_T}{qL^2}, \quad (2)$$

where V_T is the threshold voltage (44 V). A pair of gold interdigital electrodes were deposited on each facet, with a figure width of 150 μm, as shown in Fig. S6. According to the equation, a carrier mobility of 0.17 $cm^2\ V^{-1}\ s^{-1}$ was

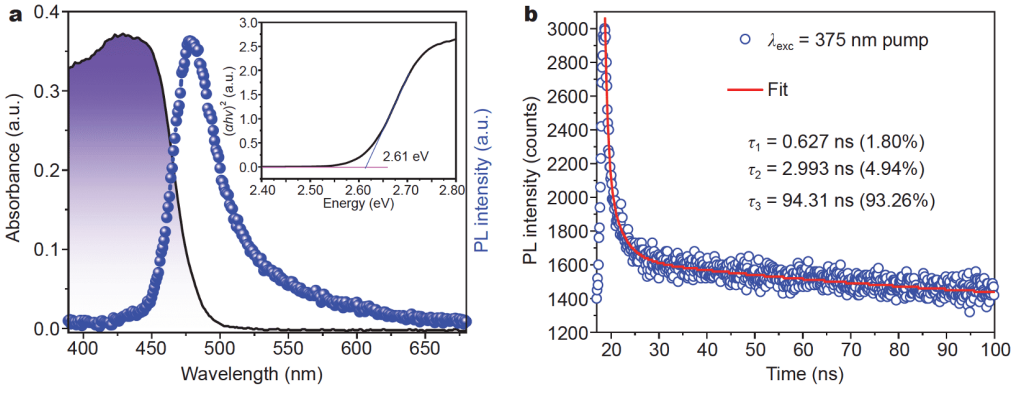

Figure 3 (a) Absorption and fluorescence emission spectra of $Cs_3Bi_2Br_9$ powder. Inset: Tauc plot showing the direct bandgap of 2.61 eV. (b) Time-resolved PL decay and fitting curve of $Cs_3Bi_2Br_9$ sample.

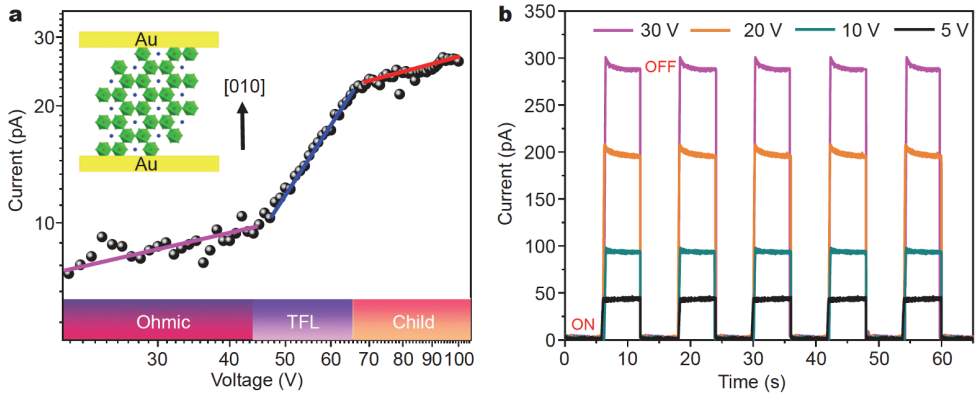

Figure 4 (a) Dark current-voltage characteristics of the (−120) plane measured using the SCLC method along the [010] direction. Inset: a sandwich structure of Au/$Cs_3Bi_2Br_9$ SC/Au. (b) Time-dependent on-off photocurrents of the (−120) plane device at bias voltages of 5, 10, 20, and 30 V under 430 nm LD illumination.

derived along the [010] direction, which can be categorized in the range of $MAPbI_3$ SC (0.61 $cm^2 V^{-1} s^{-1}$) [35], (TMHD)$BiBr_5$ SC (0.21 $cm^2 V^{-1} s^{-1}$) [11] and $Cs_2AgBiBr_6$ SC (smaller than 3.17 $cm^2 V^{-1} s^{-1}$) [34]. The low mobility may be attributed to the 'zigzag' chains constructed with $[BiBr_6]^-$ octahedra [21,36–38], which decreases the carrier transport within the (−120) plane of the $Cs_3Bi_2Br_9$ SC. Shi *et al.* [39] reported that the exciton binding energies (E_b) of $Cs_3Bi_2Br_9$ and $Cs_2AgBiBr_6$ were 322 and 85 meV, respectively. The E_b of $Cs_3Bi_2Br_9$ is significantly higher than that of $Cs_2AgBiBr_6$, which hinders the separation of excitons and the transportation of carriers for the $Cs_3Bi_2Br_9$ SC. The n_{trap} of $Cs_3Bi_2Br_9$ is 9.7 × 10^{10} cm^{-3}, which is much smaller than that of $(H_2MDAP)BiI_5$ (n_{trap} = 3.6 × 10^{11} cm^{-3}) [21] and falls in the range of that of $Rb_3Bi_2I_9$ (n_{trap} = 8.43×10^{10} cm^{-3}) [24]. In addition, the mobility lifetime ($\mu\tau$) is shown in Fig. S7. The $\mu\tau$ product of the $Cs_3Bi_2Br_9$ SC perpendicular to the (−120) plane is 3.73×10^{-5} $cm^2 V^{-1}$, which is slightly smaller than that of $Rb_3Bi_2I_9$ (9.43×10^{-4} $cm^2 V^{-1}$) [24].

From the wavelength-dependent current curve of the (−120) plane (Fig. S8), we can observe that the current has a maximum value at 430 nm. Thus, the optimal excitation wavelength was determined to be 430 nm for the $Cs_3Bi_2Br_9$ SC device. Fig. 4b shows the time-dependent response curves of the (−120) plane illuminated by a 430 nm LD with a power density of 14.9 mW mm^{-2} at bias voltages of 5, 10, 20 and 30 V. The amperometric *I-T* curves demonstrate that the device can repeatedly produce stable photocurrent signals in response to periodic switching of the light. A dark current density of ~1.03 pA mm^{-2} was obtained for a 30 V bias, which is significantly lower than that of $CsPbBr_3$ (29 nA mm^{-2}) [7]. The ultra-low dark current reflects the high resistivity (~6.8×10^{11} Ω cm) of a melt-grown $Cs_3Bi_2Br_9$ SC with high purity. For a voltage of 30 V, the on-off ratio of the $Cs_3Bi_2Br_9$ SC photoresponse device is higher than 150, which is larger than that of other bismuth-based perovskites, such as Cs_3BiBr_6 and $Cs_3Bi_2I_9$ SCs [23,40] (Table S3).

The dark current and photocurrent of the (−120) plane, dependent on voltage, are shown in Fig. S9. The *I-V* curves, which represent good ohmic contact between the Au electrode and $Cs_3Bi_2Br_9$ SC, exhibit typical linear and symmetrical behaviors. The dark current was only ~1.029 pA mm^{-2} for the (−120) plane at a 20 V bias. Moreover, the photocurrent steeply increases as the bias voltage is enhanced from −20 to 20 V. As the power density increased from 2.97 to 14.9 mW mm^{-2}, the photocurrent increased from 28 to 190 pA at 20 V bias.

As shown in Fig. 5a, the attenuation efficiencies *versus* thicknesses for a few representative semiconductors to 50 keV X-ray photons were calculated using the photon cross-section database [41]. The $Cs_3Bi_2Br_9$ SC has a stronger attenuation coefficient than that of most commercial compounds. For example, the 1-mm-thick $Cs_3Bi_2Br_9$ SC is sufficient to attenuate 98.1% of the incident X-ray photons, compared with CdTe (99.4%), $MAPbBr_3$ (90.6%), α-Se (87.0%), and Si (10.6%). Fig. S10a shows the absorption coefficients of $Cs_3Bi_2Br_9$, CdTe, $MAPbBr_3$, Si, and α-Se. Owing to the high-*Z* elements of Cs, Bi, and Br, and the high density (4.7 g cm^{-3}), $Cs_3Bi_2Br_9$ SC possesses a larger X-ray absorption coefficient than $MAPbBr_3$, commercial silicon, and α-Se, and is similar to CdTe.

Fig. 5b shows the current responses *versus* the dose rates of the $Cs_3Bi_2Br_9$ SC X-ray detector for 200 V. For an X-ray dose decreasing from 5.499 to 0.786 mGy s^{-1}, the

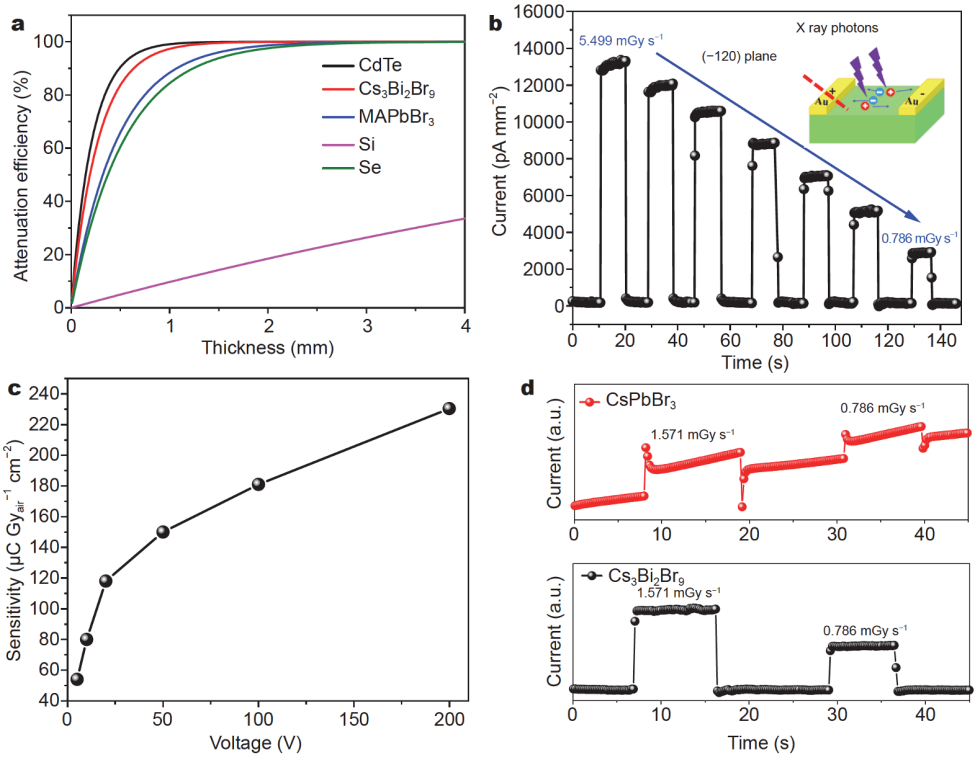

Figure 5 (a) Attenuation efficiency *versus* thickness of a few representative semiconductors to 50 keV X-ray photons. (b) The photocurrent responses for a voltage of 200 V and various dose rates of the $Cs_3Bi_2Br_9$ SC X-ray detector. Inset: the X-ray device with planar structure. (c) X-ray sensitivity of the optimized $Cs_3Bi_2Br_9$ SC for different voltages. (d) Responses of $CsPbBr_3$ (top) and $Cs_3Bi_2Br_9$ (bottom) SC-based X-ray detectors; the dose rate was set to 1.571 and 0.786 mGy s^{-1}.

photocurrent (saturated current) linearly decreased (Fig. S10b). Note that for the same voltage of 100 V, the dark current density of the $Cs_3Bi_2Br_9$ detector is as low as ~17.8 pA mm^{-2}, which is significantly lower than that of $Rb_3Bi_2I_9$ (~38.2 pA mm^{-2}) [24]. The ultra-low dark current density induces lower noise and is also beneficial to the ultra-low detection limit for X-ray detectors [20,21,25]. The inset in Fig. 5b shows the device schematic illustration of the (−120) plane with a pair of planar structured Au electrodes.

The X-ray S can be calculated using the following equation [42]:

$$S = \frac{I_{pc} - I_{dark}}{AX}, \quad (3)$$

where I_{pc} and I_{dark} are the photocurrent and dark current for the device, respectively; X is the X-ray dose, and A is the effective area of the detector.

As shown in Fig. 5c, the $Cs_3Bi_2Br_9$ SC X-ray detectors obtained an S of 54.3 μC Gy$_{air}^{-1}$ cm^{-2} at a bias voltage of 5 V, which further increased to 230.4 μC Gy$_{air}^{-1}$ cm^{-2} as the bias voltage increased to 200 V. The performance of $Cs_3Bi_2Br_9$ SC detector is superior to that of $Rb_3Bi_2I_9$ (159 μC Gy$_{air}^{-1}$ cm^{-2}) [24] and is comparable to that of $BDAPbI_4$ (242 μC Gy$_{air}^{-1}$ cm^{-2}) [8]. Moreover, the S (230.4 μC Gy$_{air}^{-1}$ cm^{-2}) is more than two times that of the $Cs_2AgBiBr_6$ SC (105 μC Gy$_{air}^{-1}$ cm^{-2}) [34], three times that of the $MAPbBr_3$ SC (80 μC Gy$_{air}^{-1}$ cm^{-2}) [43], and more than 11 times that of the α-Se SC detector (20 μC Gy$_{air}^{-1}$ cm^{-2}) [44] (Table S4). Moreover, a vertically structured Au/$Cs_3Bi_2Br_9$ SC/Au X-ray detector was also manufactured, as shown in Fig. S11a. The two Au electrodes were deposited onto the opposite (−120) plane. Fig. S11b shows the photocurrent response under 100 V and various dose rates of the $Cs_3Bi_2Br_9$ SC X-ray detector. The S of the vertical structure $Cs_3Bi_2Br_9$ SC device is 8.53 μC Gy$_{air}^{-1}$ cm^{-2}, which was calculated by fitting the slope of the line in Fig. S11c. The X-ray response S of the device with the coplanar structure was 181.2 μC Gy$_{air}^{-1}$ cm^{-2}, which is significantly higher than that of the vertical structure (8.53 μC Gy$_{air}^{-1}$ cm^{-2}) under the same testing conditions (voltage: 100 V). The S (8.53 μC Gy$_{air}^{-1}$ cm^{-2}) of the vertical structure is superior to 4.2 μC Gy$_{air}^{-1}$ cm^{-2} for the 2D double perovskite

$(BA)_2CsAgBiBr_7$ SC [20], 1 μC Gy_{air}^{-1} cm^{-2} for the $(H_2MDAP)BiI_5$ SC [21], 0.8 μC Gy_{air}^{-1} cm^{-2} for the $(CPA)_4AgBiBr_8$ SC [45], and 7.5 μC Gy_{air}^{-1} cm^{-2} for the Cd(Zn)Te SC X-ray detectors [42], which indicates the potential application for X-ray imaging [44] (Table S4). The planar structure device (electric field parallel to the (−120) plane) possesses a higher *S* than the vertically structured device (electric field perpendicular to the (−120) plane), owing to anisotropic charge transport. Thus, when the (−120) plane of the $Cs_3Bi_2Br_9$ SC was irradiated by X-rays, the charge transport benefitted from the planar structure instead of the vertical structure.

Fig. 5d shows the baseline (dark current) of a vertically structured Au/$Cs_3Bi_2Br_9$ SC/Au X-ray detector device, which does not exhibit any drift in the photocurrent response measurement, even for a high voltage of 50 V. In comparison, for the same voltage, the dark current baseline shift of a vertically structured Au/$CsPbBr_3$ SC/Au X-ray detector device for the photocurrent response measurement is severe. Typically, the baseline drift is related to the ionic migration of halide perovskites, which is detrimental to the long-term stability of the device properties. In particular, a high voltage typically damages the ordered structure and causes a structural distortion of the crystal materials, resulting in photocurrent decay, hysteresis, and baseline drift [25,46,47]. The utilization of low-dimension perovskites is a promising strategy to overcome the ionic motion of crystal materials, and many low-dimensional lead- and bismuth-halide perovskites, such as $Rb_3Bi_2I_9$ SC (2D), $(PEA)_2PbI_4$ SC (2D), $MA_3Bi_2I_9$ SC (0D), and $(NH_4)_3Bi_2I_9$ SC (2D), exhibit larger ionic motion activation energies than the conventional related 3D perovskites [4,25,48]. Therefore, we hypothesize that the no-drift baseline of the $Cs_3Bi_2Br_9$ SC revealed the weak ionic migration feature.

CONCLUSIONS

In summary, high-quality transparent bismuth-halide perovskite $Cs_3Bi_2Br_9$ SCs with a diameter of 12 mm and the length of 40 mm were grown using the modified Bridgman method. The crystal exhibits good thermal stability, as high as 500°C, and an ultra-wide transmittance range, from 0.48 μm to more than 18 μm. The carrier mobility of the $Cs_3Bi_2Br_9$ SC along the [010] orientation is 0.17 cm^2 V^{-1} s^{-1}, and the n_{trap} is 9.7×10^{10} cm^{-3}. Remarkably, the superior X-ray *S* of 230.4 μC Gy_{air}^{-1} cm^{-2} and the ultra-low and no-drift dark current density of ~17.8 pA mm^{-2} indicate that the $Cs_3Bi_2Br_9$ SC is a promising candidate for X-ray medical imaging and security screening applications.

Received 27 August 2020; accepted 2 November 2020; published online 4 January 2021

1 Xue J, Yang D, Cai B, *et al.* Photon-induced reversible phase transition in $CsPbBr_3$ perovskite. Adv Funct Mater, 2019, 29: 1807922
2 Yan G, Ji Z, Li Z, *et al.* All-inorganic $Cs_2AgBiBr_6$/CuSCN-based photodetectors for weak light imaging. Sci China Mater, 2021, 64: 198–208
3 Wang Y, Yang D, Ma D, *et al.* Organic-inorganic hybrid Sn-based perovskite photodetectors with high external quantum efficiencies and wide spectral responses from 300 to 1000 nm. Sci China Mater, 2019, 62: 790–796
4 Zhuang R, Wang X, Ma W, *et al.* Highly sensitive X-ray detector made of layered perovskite-like $(NH_4)_3Bi_2I_9$ single crystal with anisotropic response. Nat Photonics, 2019, 13: 602–608
5 Chen Z, Li C, Zhumekenov AA, *et al.* Solution-processed visible-blind ultraviolet photodetectors with nanosecond response time and high detectivity. Adv Opt Mater, 2019, 7: 1900506
6 Zhang Q, Tavakoli MM, Gu L, *et al.* Efficient metal halide perovskite light-emitting diodes with significantly improved light extraction on nanophotonic substrates. Nat Commun, 2019, 10: 727
7 Zhang P, Zhang G, Liu L, *et al.* Anisotropic optoelectronic properties of melt-grown bulk $CsPbBr_3$ single crystal. J Phys Chem Lett, 2018, 9: 5040–5046
8 Shen Y, Liu Y, Ye H, *et al.* Centimeter-sized single crystal of two-dimensional halide perovskites incorporating straight-chain symmetric diammonium ion for X-ray detection. Angew Chem Int Ed, 2020, 59: 14896–14902
9 Yang WS, Noh JH, Jeon NJ, *et al.* High-performance photovoltaic perovskite layers fabricated through intramolecular exchange. Science, 2015, 348: 1234–1237
10 Leng M, Yang Y, Zeng K, *et al.* All-inorganic bismuth-based perovskite quantum dots with bright blue photoluminescence and excellent stability. Adv Funct Mater, 2018, 28: 1704446
11 Ji C, Wang P, Wu Z, *et al.* Inch-size single crystal of a lead-free organic-inorganic hybrid perovskite for high-performance photodetector. Adv Funct Mater, 2018, 28: 1705467
12 Tong XW, Zhang ZX, Wang D, *et al.* Inorganic $CsBi_3I_{10}$ perovskite/silicon heterojunctions for sensitive, self-driven and air-stable NIR photodetectors. J Mater Chem C, 2019, 7: 863–870
13 Wang Y, Wen R, Liu Y, *et al.* Rigid amine-induced pseudo-3D lead-free bismuth halide perovskite with an improved band edge for visible-light absorption. ChemSusChem, 2020, 13: 2753–2760
14 Lee B, Stoumpos CC, Zhou N, *et al.* Air-stable molecular semiconducting iodosalts for solar cell applications: Cs_2SnI_6 as a hole conductor. J Am Chem Soc, 2014, 136: 15379–15385
15 Lehner AJ, Fabini DH, Evans HA, *et al.* Crystal and electronic structures of complex bismuth iodides $A_3Bi_2I_9$ (A = K, Rb, Cs) related to perovskite: Aiding the rational design of photovoltaics. Chem Mater, 2015, 27: 7137–7148
16 Saparov B, Hong F, Sun JP, *et al.* Thin-film preparation and characterization of $Cs_3Sb_2I_9$: A lead-free layered perovskite semiconductor. Chem Mater, 2015, 27: 5622–5632
17 Mohan R. Green bismuth. Nat Chem, 2010, 2: 336
18 Wu C, Zhang Q, Liu G, *et al.* From Pb to Bi: A promising family of Pb-free optoelectronic materials and devices. Adv Energy Mater, 2020, 10: 1902496
19 Zheng X, Zhao W, Wang P, *et al.* Ultrasensitive and stable X-ray detection using zero-dimensional lead-free perovskites. J Energy

Chem, 2020, 49: 299–306
20 Xu Z, Liu X, Li Y, *et al.* Exploring lead-free hybrid double perovskite crystals of $(BA)_2CsAgBiBr_7$ with large mobility-lifetime product toward X-ray detection. Angew Chem Int Ed, 2019, 58: 15757–15761
21 Tao K, Li Y, Ji C, *et al.* A lead-free hybrid iodide with quantitative response to X-ray radiation. Chem Mater, 2019, 31: 5927–5932
22 Zhang Y, Liu Y, Xu Z, *et al.* Nucleation-controlled growth of superior lead-free perovskite $Cs_3Bi_2I_9$ single-crystals for high-performance X-ray detection. Nat Commun, 2020, 11: 2304
23 Sun Q, Xu Y, Zhang H, *et al.* Optical and electronic anisotropies in perovskitoid crystals of $Cs_3Bi_2I_9$ studies of nuclear radiation detection. J Mater Chem A, 2018, 6: 23388–23395
24 Xia M, Yuan J, Niu G, *et al.* Unveiling the structural descriptor of $A_3B_2X_9$ perovskite derivatives toward X-ray detectors with low detection limit and high stability. Adv Funct Mater, 2020, 30: 1910648
25 Liu Y, Xu Z, Yang Z, *et al.* Inch-size 0D-structured lead-free perovskite single crystals for highly sensitive stable X-ray imaging. Matter, 2020, 3: 180–196
26 Ji Z, Liu Y, Li W, *et al.* Reducing current fluctuation of $Cs_3Bi_2Br_9$ perovskite photodetectors for diffuse reflection imaging with wide dynamic range. Sci Bull, 2020, 65: 1371–1379
27 Gao M, Zhang C, Lian L, *et al.* Controlled synthesis and photostability of blue emitting $Cs_3Bi_2Br_9$ perovskite nanocrystals by employing weak polar solvents at room temperature. J Mater Chem C, 2019, 7: 3688–3695
28 Lou Y, Fang M, Chen J, *et al.* Formation of highly luminescent cesium bismuth halide perovskite quantum dots tuned by anion exchange. Chem Commun, 2018, 54: 3779–3782
29 Yang B, Chen J, Hong F, *et al.* Lead-free, air-stable all-inorganic cesium bismuth halide perovskite nanocrystals. Angew Chem, 2017, 129: 12645–12649
30 Bass KK, Estergreen L, Savory CN, *et al.* Vibronic structure in room temperature photoluminescence of the halide perovskite $Cs_3Bi_2Br_9$. Inorg Chem, 2017, 56: 42–45
31 Tang Y, Liang M, Chang B, *et al.* Lead-free double halide perovskite Cs_3BiBr_6 with well-defined crystal structure and high thermal stability for optoelectronics. J Mater Chem C, 2019, 7: 3369–3374
32 Fang Y, Dong Q, Shao Y, *et al.* Highly narrowband perovskite single-crystal photodetectors enabled by surface-charge recombination. Nat Photon, 2015, 9: 679–686
33 Yang B, Pan W, Wu H, *et al.* Heteroepitaxial passivation of $Cs_2AgBiBr_6$ wafers with suppressed ionic migration for X-ray imaging. Nat Commun, 2019, 10: 1989
34 Pan W, Wu H, Luo J, *et al.* $Cs_2AgBiBr_6$ single-crystal X-ray detectors with a low detection limit. Nat Photon, 2017, 11: 726–732
35 Song Y, Bi W, Wang A, *et al.* Efficient lateral-structure perovskite single crystal solar cells with high operational stability. Nat Commun, 2020, 11: 274
36 Kagan CR, Mitzi DB, Dimitrakopoulos CD. Organic-inorganic hybrid materials as semiconducting channels in thin-film field-effect transistors. Science, 1999, 286: 945–947
37 Gao JX, Hua XN, Chen XG, *et al.* $[C_6N_2H_{18}][SbI_5]$: A lead-free hybrid halide semiconductor with exceptional dielectric relaxation. Inorg Chem, 2019, 58: 4337–4343
38 Zhang W, Tao K, Ji C, *et al.* $(C_6H_{13}N)_2BiI_5$: A one-dimensional lead-free perovskite-derivative photoconductive light absorber. Inorg Chem, 2018, 57: 4239–4243
39 Shi M, Li G, Tian W, *et al.* Understanding the effect of crystalline structural transformation for lead-free inorganic halide perovskites. Adv Mater, 2020, 32: 2002137
40 Zhang H, Xu Y, Sun Q, *et al.* Lead free halide perovskite $Cs_3Bi_2I_9$ bulk crystals grown by a low temperature solution method. CrystEngComm, 2018, 20: 4935–4941
41 Berger MJ, et al. XCOM: Photon Cross Sections Database: NIST Standard Reference Database 8 (NIST, 2013). https://www.nist.gov/pml/xcom-photoncross-sections-database
42 Dvoryankin VF, Dvoryankina GG, Kudryashov AA, *et al.* X-ray sensitivity of $Cd_{0.9}Zn_{0.1}Te$ detectors. Tech Phys, 2010, 55: 306–308
43 Wei H, Fang Y, Mulligan P, *et al.* Sensitive X-ray detectors made of methylammonium lead tribromide perovskite single crystals. Nat Photon, 2016, 10: 333–339
44 Kasap SO. X-ray sensitivity of photoconductors: Application to stabilized a-Se. J Phys D-Appl Phys, 2000, 33: 2853–2865
45 Guo W, Liu X, Han S, *et al.* Room-temperature ferroelectric material composed of a two-dimensional metal halide double perovskite for X-ray detection. Angew Chem, 2020, 132: 13983–13988
46 Li C, Tscheuschner S, Paulus F, *et al.* Iodine migration and its effect on hysteresis in perovskite solar cells. Adv Mater, 2016, 28: 2446–2454
47 Lin Y, Bai Y, Fang Y, *et al.* Suppressed ion migration in low-dimensional perovskites. ACS Energy Lett, 2017, 2: 1571–1572
48 Liu Y, Ye H, Zhang Y, *et al.* Surface-tension-controlled crystallization for high-quality 2D perovskite single crystals for ultrahigh photodetection. Matter, 2019, 1: 465–480

Acknowledgements This work was supported by the National Natural Science Foundation of China (51972194, 51602178, 51932004 and 61975098), the 111 Project 2.0 (BP2018013), the National Key Research and Development Program of China (2016YFB1102201 and 2018YFB0406502), the Fundamental Research Funds of Shandong University, the State Key Laboratory of Solidification Processing in Northwestern Polytechnical University (NWPU) (SKLSP202019), and Shandong Provincial Key Research and Development Program (2018GGX102003).

Author contributions Zhang G and Tao X conceived the idea and obtained the research grants; Li X designed the experiments, synthesized the materials, conducted the characterizations, and wrote the manuscript; Zhang P and Liu L reviewed the manuscript; Hua Y contributed to the general discussion and measurements; Du X, Niu G, and Tang J conceived the discussion and conducted the X-ray detection measurements. All authors contributed to the general discussion.

Conflict of interest The authors declare that they have no conflict of interest.

Supplementary information Supporting data and calculation details are available in the online version of the paper.

Xiang Li received his BSc (Honors) degree in 2018 from the Harbin University of Science and Technology of China and is a Master student at Shandong University. His research focuses on photoelectric and X-ray detection studies of $Cs_3Bi_2Br_9$ single crystals.

Guodong Zhang obtained his PhD degree in 2012 from Shandong University. He is an associate professor at the Institute of Crystal Materials, Shandong University. His main interests focus on the growth of halide and phosphide single crystals for radiation detection, infrared acoustic-optical applications, and infrared nonlinear optical applications.

Xutang Tao obtained his PhD degree in 1995 from Tokyo University of Agriculture and Technology, Japan. He is a chief professor at the Institute of Crystal Materials, Shandong University. His main interests include lasers, nonlinear optical crystals, wide-gap semiconductors, and all-inorganic and organic-inorganic hybrid perovskite optoelectronic functional materials and devices.

用于高性能X射线探测的无铅卤化物钙钛矿$Cs_3Bi_2Br_9$单晶

李想[1†], 杜鑫源[2†], 张鹏[1], 华云秋[1], 刘琳[1], 牛广达[2*], 张国栋[1*], 唐江[2], 陶绪堂[1*]

摘要 近年来, 全无机无铅卤化物钙钛矿以其良好的环境稳定性和热稳定性、优异的光电性能以及环境友好性而受到广泛关注. 本文采用改进的垂直布里奇曼法首次生长出直径12 mm、长度约40 mm、透明性良好的$Cs_3Bi_2Br_9$单晶. 生长的$Cs_3Bi_2Br_9$单晶的电阻率约为6.8×10^{11} Ω cm, 透过率约为80%. 在(−120)晶面内, 载流子迁移率为0.17 $cm^2 V^{-1} s^{-1}$, 缺陷态密度为9.7×10^{10} cm^{-3}. 在X射线探测方面, $Cs_3Bi_2Br_9$单晶最大灵敏度约为230.4 μC Gy_{air}^{-1} cm^{-2}; 暗电流密度约为17.8 pA mm^{-2}, 且没有漂移现象, 这表明$Cs_3Bi_2Br_9$单晶具有更小的暗电流噪声, 有利于获得更低的检测限.